ISSN 1070-3632, Russian Journal of General Chemistry, 2024, Vol. 94, No. 6, pp. 1309–1321. © Pleiades Publishing, Ltd., 2024.

Relationship between the Composition and Structural Characteristics of Catalysts Based on Calcium Ferrites and Their Activity with Respect to Hydrogen

N. P. Kirik[a],*, V. V. Yumashev[a], O. A. Bayukov[b], Yu. V. Knyazev[b], L. A. Solovyev[a], N. N. Shishkina[a], E. V. Rabchevskii[a], and A. G. Anshits[a]

[a] *Institute of Chemistry and Chemical Technology, Federal Krasnoyarsk Research Center, Siberian Branch, Russian Academy of Sciences, Krasnoyarsk, 660036 Russia*
[b] *Kirensky Institute of Physics, Federal Krasnoyarsk Research Center, Siberian Branch, Russian Academy of Sciences, Krasnoyarsk, 660036 Russia*
**e-mail: kiriknp@icct.ru*

Received May 28, 2024; revised May 28, 2024; accepted June 27, 2024

Abstract—Using the methods of X-ray diffraction, Mössbauer spectroscopy, and temperature-programmed reduction with hydrogen, the relationship between the phase composition, structural characteristics of the phases, and the reactivity with respect to hydrogen was investigated for calcium ferrites-based catalysts. The catalyst samples were prepared via solid-state synthesis from CaO and Fe_2O_3 at 900 and 1000°C by varying the Fe_2O_3 content in the CaO–Fe_2O_3 system. The phase composition of the resultant samples corresponds to the CaO–$Ca_2Fe_2O_5$, $Ca_2Fe_2O_5$–$CaFe_2O_4$, and $CaFe_2O_4$–α-Fe_2O_3 regions. In the CaO–$Ca_2Fe_2O_5$ samples the lattice parameters of $Ca_2Fe_2O_5$ and its activity with respect to hydrogen depend on the phase ratio. The activity of $CaFe_2O_4$ is higher in $Ca_2Fe_2O_5$–$CaFe_2O_4$ compared to $CaFe_2O_4$–α-Fe_2O_3 catalysts.

Keywords: calcium ferrites, solid-state synthesis, X-ray diffraction, Mössbauer spectroscopy, TPR-H_2

DOI: 10.1134/S1070363224060094

INTRODUCTION

Stoichiometric oxides and two-phase compositions formed in the CaO–Fe_2O_3 system hold promise as catalysts for oxidation processes, so-called oxygen carriers in high-temperature chemical looping (CL) processes, and also as gas sensors and membranes and materials for electrochemical systems.

The end-members of the CaO–Fe_2O_3 system, simple oxides CaO and Fe_2O_3, exhibit catalytic properties in oxidative conversion of lower hydrocarbons, CO, and H_2. Specifically, CaO at 750°C is active in the oxidative coupling of methane (OCM) with an overall selectivity of 61% to partial oxidation products such as C_2 hydrocarbons and CO [1]. Upon CaO lattice doping with Li (0.4 at %) [2] and La (0.2 at %) [3] ions the activity increases threefold and by more than two orders of magnitude, respectively. Oxide α-Fe_2O_3 at moderate temperatures (350–400°C) catalyzes deep oxidation of H_2, methane, and other lower hydrocarbons [4]. Modification of α-Fe_2O_3 with γ-Al_2O_3 oxide leads to an effective catalyst for CO oxidation [5].

In the CaO–Fe_2O_3 system, stable complex oxides such as stoichiometric calcium ferrites $Ca_2Fe_2O_5$ and $CaFe_2O_4$ can be formed [6]. They are characterized by high-temperature stability, low thermal expansion coefficients, ability to transport oxygen ions, and mixed ion-electron (mainly electron, *p*-type) conductivity [7, 8]. Owing to these properties, calcium ferrites and systems on their basis are the focus of investigation for possible uses as electrodes in fuel cells and Li-ion batteries, gas sensors, and photocatalysts [9–12].

Also, the catalytic properties of calcium ferrites and calcium ferrites-based systems are being studied [13–15]. The activity of these catalysts was shown to be dependent on the Ca/Fe atomic ratio. For example, in propylene combustion the calcium ferrite-based catalyst with Ca/Fe = 1 ($Ca_2Fe_2O_5$ main phase) displayed higher activity compared to those with Ca/Fe = 0.5 ($CaFe_2O_4$ main phase)

Table 1. Phase composition and specific surface area of the $CaO–Fe_2O_3$ system catalysts (T_{syn} = 1000°C)

Fe_2O_3 wt %	Phase content, wt %				S_{sp}, m^2/g
	CaO	$Ca_2Fe_2O_5$	$CaFe_2O_4$	α-Fe_2O_3	
0	100				0.79
10	85	15			0.87
20	68	32			0.97
25	59	41			0.82
35	40	60			0.88
45	25	74	1		1.02
55	5	91	4		0.77
59	1	91	8		0.54
60		81	19		0.49
65		51	49		0.56
70		18	82		0.64
74			98	2	0.53
78			81	19	0.55
80			73	27	0.73
85			55	45	0.50
90			33	67	0.42
95			18	82	0.17
100				100	0.27

and Ca/Fe = 2 [$Ca(OH)_2$ and $Ca_2Fe_2O_5$ main phases] [13]. In the catalytic oxidation of 1,2-dichlorobenzene, the greatest activity in the series of catalysts represented by Ca-doped FeO_x hollow microspheres (0–20 mol % Ca) was exhibited by the sample containing 9.7 mol % Ca [15].

Systems containing iron oxides and calcium ferrites are intensively studied as oxygen carriers for high-temperature (≥800°C) CL processes such as fuel combustion [16, 17], partial methane oxidation [18], hydrogen generation [19–21], gasification of coal and biomass [22, 23], and production of biodiesel fuel [24]. In CL processes, carbonaceous feedstock is oxidized by the lattice oxygen from oxygen carriers in the first stage, whereupon the reduced oxygen carrier is re-oxidized in the presence of O_2, H_2O, or CO_2. The redox properties of oxygen carriers are essential for their use in cyclic processes. The main advantages offered by oxygen carrier systems based on iron oxides and calcium ferrites over other oxide systems are high oxygen capacity, possibility of modifying the reactivity, high melting temperature, good mechanical strength characteristics, low cost, and natural compatibility.

The activity of calcium ferrites-based systems in various processes was the focus of numerous research publications. At the same time, there were no systematic and comprehensive studies on the influence of the phase composition of the $CaO–Fe_2O_3$ oxide system catalysts, in which the contents of the components vary over a wide range, and of the structural characteristics of the phases on the activity of such catalysts in oxidation processes. In this study, we investigated the relationship between, on the one hand, the phase composition, structural and microstructural characteristics of the phases, and the state of Fe ions in the $CaO–Fe_2O_3$ system catalysts with the Fe_2O_3 content varied over the entire 0 to 100 wt % range and, on the other hand, their reactivity towards hydrogen in a temperature-programmed reduction reaction.

RESULTS AND DISCUSSION

Phase Composition of the Catalysts. In the $CaO–Fe_2O_3$ oxide system at 900–1000°C under variation of the Fe_2O_3 content from 0 to 100 wt %, according to the equilibrium phase diagram in an air atmosphere, the 0–58.7, 58.7–74, and 74–100 wt % Fe_2O_3 composition ranges correspond to the $CaO–Ca_2Fe_2O_5$, $Ca_2Fe_2O_5–CaFe_2O_4$, and $CaFe_2O_4$–α-Fe_2O_3 phase composition regions, respectively [6]. Table 1 presents the XRD data obtained in this study for the catalysts synthesized at 1000°C (4 h). It is seen that the $CaO–Fe_2O_3$ blend containing 10–35 wt % Fe_2O_3 gives two-phase samples represented by the CaO and $Ca_2Fe_2O_5$ phases. With increasing Fe_2O_3 content the $Ca_2Fe_2O_5$ phase content increases from 15 to 60%, and that of the CaO phase decreases from 85 to 40%. When the Fe_2O_3 content in the blend increases to 45–59 wt %, up to 8 wt % $CaFe_2O_4$ ferrite phase is also detected in the samples (Table 1). The blend containing 60–70 wt % Fe_2O_3 gives two-phase samples from the $Ca_2Fe_2O_5–CaFe_2O_4$ region. At Fe_2O_3 content ≥74 wt % the formation of $CaFe_2O_4$–α-Fe_2O_3 two-phase samples, having the α-Fe_2O_3 phase content widely varying from 2 to 82 wt %, is observed. Earlier [25], we reported on the formation under the actual synthesis conditions of core–shell samples of the structured composite materials $CaFe_2O_4$–α-Fe_2O_3, where the α-Fe_2O_3 phase acts as the core. The specific surface area (S_{sp}) of all the obtained calcium ferrite catalysts (Table 1), except for 95% Fe_2O_3 sample, varies within 0.4–1.0 m^2/g, with a larger surface area of ~0.8–1.0 m^2/g exhibited by the $CaO–Ca_2Fe_2O_5$ samples.

Table 2. Phase composition and specific surface area of the $CaO–Fe_2O_3$ system catalysts (T_{syn} = 900°C)

Fe_2O_3, wt %	Phase content, wt %				S_{sp}, m^2/g
	CaO	$Ca_2Fe_2O_5$	$CaFe_2O_4$	α-Fe_2O_3	
0	100				0.79
20	69	28	3		0.89
35	41	56	3		1.46
45	19	79	2		1.32
50	15	81	4		1.36
55	8	83	9		1.12
60		87	13		0.83
65		48	52		0.76
70		17	83		0.90
74			98.5	1.5	1.03
75			93	7	0.77
78			85	15	1.49
80			73	27	0.89
85			55	45	0.98
90			36	64	0.83
95			19	81	0.80
100				100	0.68

The phase composition of the catalysts from the $Ca_2Fe_2O_5–CaFe_2O_4$ and $CaFe_2O_4$–α-Fe_2O_3 regions, obtained at the synthesis temperature decreased to 900°C under simultaneous increase in the synthesis time to 10 h agrees well with that of the high-temperature samples (Table 2). A difference was exhibited by the low-temperature samples from the $CaO–CaFe_2O_5$ region, all of which contain up to 9 wt % $CaFe_2O_4$ ferrite phase. Compared to the high-temperature samples, the catalysts synthesized at 900°C have a slightly higher specific surface area varying in the range 0.8–1.5 m^2/g.

Thus, the contents of phases, revealed in the catalysts synthesized at 900 and 1000°C, are overall consistent with the phase diagram of the $CaO–Fe_2O_3$ system [6]. The presence of the $CaFe_2O_4$ phase in the $CaO–Ca_2Fe_2O_5$ samples is due to kinetic limitations because of the formation of $Ca_2Fe_2O_5$ ferrite via that of $CaFe_2O_4$ ferrite [26]. Apparently, for this same reason we failed to obtain single-phase $Ca_2Fe_2O_5$ under the chosen conditions using the actual synthesis technique at a stoichiometric content of the oxides in the initial blend. As shown in [27], through a long, 150 h ceramic synthesis process at a higher temperature of 1100°C, with repeated grinding steps, it is possible to obtain nearly single-phase $Ca_2Fe_2O_5$ from the corresponding oxides.

Structural and microstructural characteristics of the iron-containing phases. The above-discussed results show that the $CaO–Fe_2O_3$ system catalysts synthesized at temperatures of 900–1000°C (by varying the hematite content from 0 to 100 wt %) include two-phase compositions from the $CaO–Ca_2Fe_2O_5$ (with a $CaFe_2O_4$ admixture), $Ca_2Fe_2O_5–CaFe_2O_4$, and $CaFe_2O_4$–α-Fe_2O_3regions with different phase ratios.

For revealing possible influence of the phases in the two-phase $CaO–Fe_2O_3$ system catalysts and the presence of structural defects in the formed phases, the crystal lattice parameters of all the iron-containing phases were calculated from the XRD data.

Figure 1 presents the crystal lattice parameters of the $Ca_2Fe_2O_5$, $CaFe_2O_4$, and α-Fe_2O_3 phases in the samples synthesized at two temperatures. It seen that some differences between the lattice parameters of calcium ferrite $Ca_2Fe_2O_5$ in the predominantly two-phase samples from the $CaO–Ca_2Fe_2O_5$ region appear with an increase in the content of the ferrite phase (Tables 1 and 2, Fig. 1). Specifically, in the samples calcined at 1000°C the parameters *a* and *c* in $Ca_2Fe_2O_5$ exhibit increases in the respective ranges of 5.5896(6)–5.5941(3) and 5.4192(7)–5.4235(3) Å, and parameter *b* shows a decrease in the 14.793(3)–14.778(2) Å range. The parameters of ferrite $Ca_2Fe_2O_5$in the samples calcined at 900°C display similar trends, with the values of the parameters *a* and *c* being slightly smaller, and those of parameter *b*, larger compared to the high-temperature samples.

In the $Ca_2Fe_2O_5–CaFe_2O_4$ samples the lattice parameters of the ferrites change negligibly. For the samples calcined at 1000°C the lattice parameters *a*, *b*, and *c* of $Ca_2Fe_2O_5$ are around 5.5944, 14.7770, and 5.4237 Å, respectively. The parameters of $Ca_2Fe_2O_5$ in the $CaO–Ca_2Fe_2O_5$ samples tend to these specific values, as seen from Fig. 1. The lattice parameters *a, b*, and *c* of $CaFe_2O_4$ ferrite are around 9.2245, 3.0196, and 10.6995 Å, respectively. The calcination temperature employed in the synthesis of this group of catalysts affects mainly the lattice parameters of ferrite $Ca_2Fe_2O_5$, whose patterns of changes are analogous with those for the $CaO–Ca_2Fe_2O_5$ samples. From the results obtained it follows that, with an increase in the synthesis temperature of the $Ca_2Fe_2O_5$-containing samples, the unit cell of ferrite $Ca_2Fe_2O_5$ is compressed along the axis *b* and stretched in the perpendicular plane. This trend revealed for the

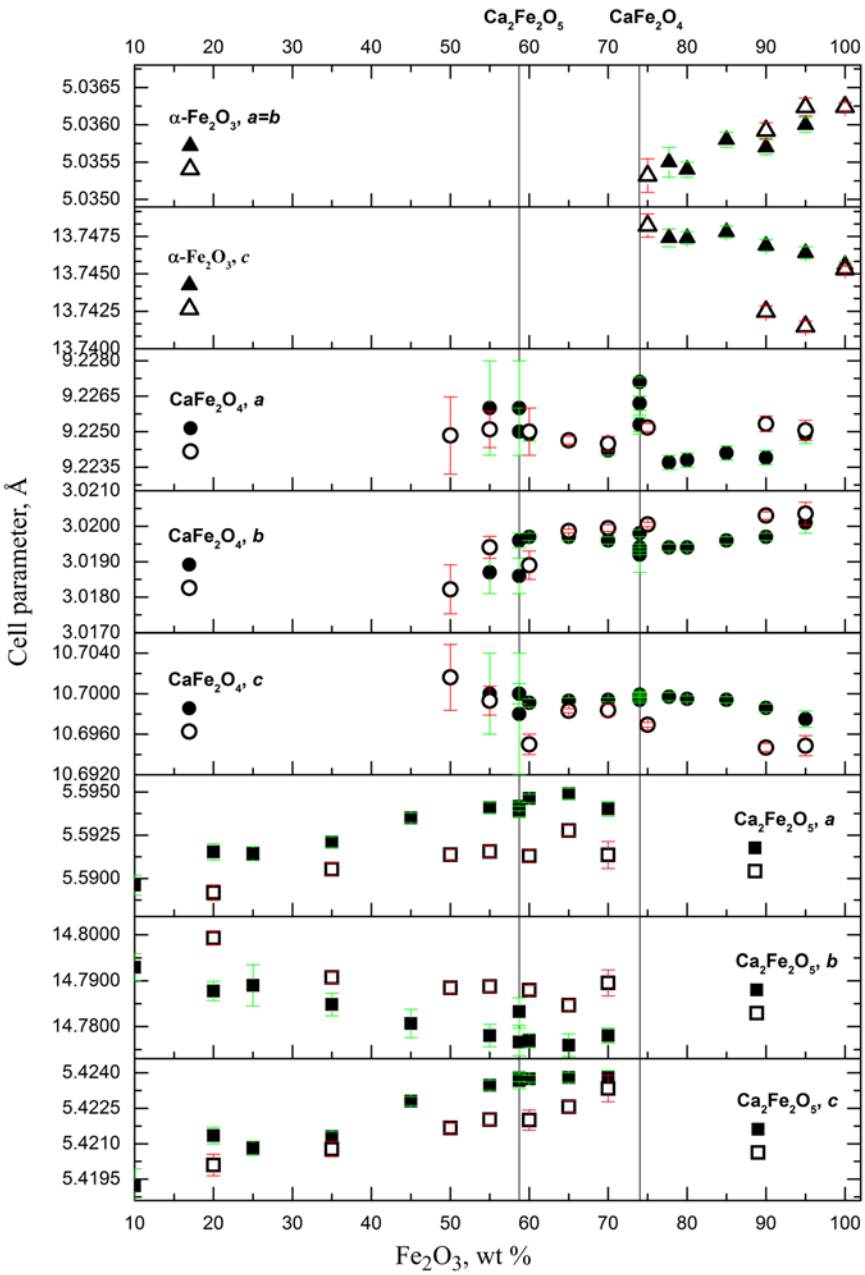

Fig. 1. Variation of the unit cell parameters of the phases in the catalysts depending on the Fe_2O_3 content in the $CaO–Fe_2O_3$ system: (hollow symbols) T_{syn} = 900°C and (solid symbols) T_{syn} = 1000°C.

unit cell of $Ca_2Fe_2O_5$is consistent with the values of the lattice parameters reported in [7] for the $Ca_2Fe_2O_5$ ferrite synthesized at a higher temperature, 1150°C.

In the two-phase samples from the $CaFe_2O_4$–α-Fe_2O_3 region (1000°C) the lattice parameters of ferrite $CaFe_2O_4$ exhibit slightly more variation, with parameters *a* and *b* negligibly increasing in the respective ranges of 9.2237(3)–9.2249(4) and 3.0194(1)–3.0201(3) and parameter *c* decreasing in the range of 10.6997(4)–10.6975(8) Å. In these samples, the lattice parameters of the second phase α-Fe_2O_3, *a* = *b* and *c*, vary slightly in the respective ranges of 5.0355(2)–5.0360(1) and 13.7474(6)–13.7464(4) Å. As we showed earlier [28], the calcination temperature affects the lattice parameters of the single-phase α-Fe_2O_3 samples, leading to a monotonous decrease in the cell volume with temperature increasing in the 800–1100°C range.

Thus, the analysis of the crystal lattice parameters of the iron-containing phases in the obtained $CaO–Fe_2O_3$ system catalysts showed that the mutual influence of the phases in the two-phase compositions is more pronounced in the case of the $CaO–Ca_2Fe_2O_5$ samples. The revealed variation of the lattice parameters of calcium ferrite $Ca_2Fe_2O_5$ depending on the $CaO/Ca_2Fe_2O_5$ ratio in the sample may be due to partial dissolution of CaO in $Ca_2Fe_2O_5$ with formation of cationic Fe vacancies and localization of holes, *h* [29]. This assumption can be supported by negligible changes of the crystal lattice parameters of ferrite Ca_2Fe_2O in the two-phase compositions from the $Ca_2Fe_2O_5–CaFe_2O_4$ region, which is well explained by the fact that solid solutions are not formed in the $CaFe_2O_4–Ca_2Fe_2O_5$ oxide system, as established in [30].

State of the iron ions and their quantitative ratio in the phases of the $CaO–Fe_2O_3$ system catalyst. For elucidating the state (charge, coordination, and vacancy states) of the iron ions and their distribution between the phases identified by XRD analysis, the synthesized samples were investigated by Mössbauer spectroscopy.

According to literature data, calcium ferrite $Ca_2Fe_2O_5$ has an orthorhombic brownmillerite structure (space group *Pnma*), which can be viewed as an anion-deficient perovskite with alternating layers of corner sharing FeO_4 and FeO_6, stacked along the *b* axis. The FeO_4 layers contain oxygen vacancies ordered parallel to the (010) planes [7]. At temperatures of 677–727°C, the space group symmetry changes from that of primitive to body-centered cell (*Pnma*→*I2mb*) [7].

Calcium ferrite $CaFe_2O_4$ also crystallizes in an orthorhombic, CaV_2O_4-type, structure (space group *Pbnm*), containing two nonequivalent iron octahedral sites, in one of which the oxygen octahedra demonstrate stronger distortion [8].

Iron oxide α-Fe_2O_3 has a hexagonal, corundum-type, structure (space group *R-3c*), where each iron atom is octahedrally coordinated to six oxygen atoms [31].

Table 3 summarizes the results of processing of the room temperature Mössbauer spectra of the catalysts containing 45–95 wt % Fe_2O_3 (T_{syn} = 900°C), whose phase composition corresponds to the $CaO–Ca_2Fe_2O_5$, $Ca_2Fe_2O_5–CaFe_2O_4$, and $CaFe_2O_4–\alpha$-Fe_2O_3 regions (Table 2). The spectra are the sums of paramagnetic doublets and Zeeman sextets. In the Mössbauer spectra of the samples containing 45–70 wt % Fe_2O_3 there are two types of sextets attributable to the tetrahedral (A) and octahedral (B) Fe sites in ferrite $Ca_2Fe_2O_5$. The spectra of the samples with >70% Fe_2O_3 exhibit one sextet with parameters characteristic of α-Fe_2O_3. The paramagnetic part of the spectra of all the catalysts is represented by two quadrupole doublets, whose parameters correspond to the $CaFe_2O_4$ ferrite phase, in which there are two Fe sites, Fe^1 and Fe^2, octahedrally coordinated to six oxygen atoms, which differ in the distortion degree of the local environment (Table 3). The values of the chemical shifts (*IS*), hyperfine fields (*H*), and quadrupole splittings (*QS*) of the $Ca_2Fe_2O_5$, $CaFe_2O_4$, and α-Fe_2O_3 phases (Table 3) are consistent with the literature data [7, 8, 32–34]. The *IS* and *QS* values correspond to Fe^{3+} cations in a high-spin state.

Analysis of the Mössbauer spectra of the catalysts containing 55–95% Fe_2O_3 in $CaO–Fe_2O_3$, which were synthesized at a higher temperature, 1000°C, showed that the Mössbauer parameters of the phases remain unchanged within the experimental error (Table 4).

The contents of the iron-containing phases in the synthesized catalysts, calculated from the Mössbauer data, are consistent with the XRD data; for the catalysts from the $Ca_2Fe_2O_5–CaFe_2O_4$ and $CaFe_2O_4–\alpha$-Fe_2O_3 regions both methods reveal almost linear variation of the contents of phases depending on the Fe_2O_3 content in the $CaO–Fe_2O_3$ system.

Use of the Mössbauer spectroscopy allowed identifying a number of structural features of ferrite $CaFe_2O_4$. Specifically, an occupancy difference between the nonequivalent sites of iron cations Fe^1 and Fe^2 (Tables 3 and 4) as dependent on the ferrite content in the catalyst was shown. In the samples containing 70–95% Fe_2O_3, a higher occupancy was revealed for the Fe^1 crystallographic positions. With increase in the $CaFe_2O_4$ content the occupancy difference between the Fe^1 and Fe^2 sites in the $CaFe_2O_4–\alpha$-Fe_2O_3 samples tends to increase, reaching a maximum (~6–10%) in the case of the nearly single-phase $CaFe_2O_4$ ferrite, 74% Fe_2O_3 sample (Tables 3 and 4). In going to the two-phase catalysts from the $Ca_2Fe_2O_5–CaFe_2O_4$ region the difference in occupancy between the Fe^1 and Fe^2 sites decreases, and at a Fe_2O_3 content of <70% the distribution of occupancy over nonequivalent Fe sites changes so that iron cations deficiency is observed in the other position, Fe^1.

It should be noted that an occupancy difference between the nonequivalent sites of Fe cations in the $CaFe_2O_4$ ferrite structure was revealed by previous Mössbauer

Table 3. Mössbauer parameters of the CaO–Fe_2O_3 system catalysts (T_{syn} = 900°C)[a]

Fe_2O_3, wt %	*IS*, ±0.005 mm/s	*H*, ±5 kOe	*QS*, ±0.01 mm/s	*W*, ±0.01 mm/s	*A*, ±3%	Crystallographic position
45	0.363	509	–1.10	0.29	0.47	B–$Ca_2Fe_2O_5$
	0.185	434	1.44	0.26	0.46	A–$Ca_2Fe_2O_5$
	0.374	–	0.76	0.24	0.04	Fe^1–$CaFe_2O_4$
	0.381	–	0.31	0.15	0.03	Fe^2–$CaFe_2O_4$
50	0.364	508	–1.10	0.29	0.46	B–$Ca_2Fe_2O_5$
	0.184	433	1.44	0.26	0.45	A–$Ca_2Fe_2O_5$
	0.370	–	0.76	0.17	0.05	Fe^1–$CaFe_2O_4$
	0.369	–	0.32	0.23	0.04	Fe^2–$CaFe_2O_4$
55	0.362	509	–1.10	0.28	0.45	B–$Ca_2Fe_2O_5$
	0.184	434	1.44	0.25	0.44	A–$Ca_2Fe_2O_5$
	0.374	–	0.70	0.15	0.05	Fe^1–$CaFe_2O_4$
	0.375	–	0.34	0.22	0.07	Fe^2–$CaFe_2O_4$
60	0.365	509	–1.11	0.26	0.40	B–$Ca_2Fe_2O_5$
	0.183	434	1.44	0.24	0.40	A–$Ca_2Fe_2O_5$
	0.374	–	0.74	0.20	0.08	Fe^1–$CaFe_2O_4$
	0.374	–	0.33	0.25	0.11	Fe^2–$CaFe_2O_4$
65	0.358	512	–1.08	0.27	0.25	B–$Ca_2Fe_2O_5$
	0.180	436	1.44	0.24	0.25	A–$Ca_2Fe_2O_5$
	0.375	–	0.74	0.25	0.24	Fe^1–$CaFe_2O_4$
	0.373	–	0.30	0.25	0.26	Fe^2–$CaFe_2O_4$
70	0.371	509	–1.12	0.27	0.08	B–$Ca_2Fe_2O_5$
	0.191	434	1.48	0.26	0.09	A–$Ca_2Fe_2O_5$
	0.376	–	0.72	0.28	0.46	Fe^1–$CaFe_2O_4$
	0.374	–	0.29	0.24	0.37	Fe^2–$CaFe_2O_4$
74	0.371	–	0.73	0.28	0.52	Fe^1–$CaFe_2O_4$
	0.369	–	0.29	0.25	0.45	Fe^2–$CaFe_2O_4$
78	0.381	516	–0.42	0.24	0.27	α-Fe_2O_3
	0.376	–	0.73	0.26	0.38	Fe^1–$CaFe_2O_4$
	0.372	–	0.29	0.27	0.35	Fe^2–$CaFe_2O_4$
80	0.381	516	–0.40	0.25	0.39	α-Fe_2O_3
	0.376	–	0.75	0.27	0.31	Fe^1–$CaFe_2O_4$
	0.374	–	0.30	0.28	0.30	Fe^2–$CaFe_2O_4$
85	0.383	517	–0.41	0.23	0.56	α-Fe_2O_3
	0.377	–	0.72	0.28	0.23	Fe^1–$CaFe_2O_4$
	0.372	–	0.29	0.25	0.21	Fe^2–$CaFe_2O_4$
90	0.377	517	–0.41	0.24	0.69	α-Fe_2O_3
	0.375	–	0.73	0.26	0.17	Fe^1–$CaFe_2O_4$
	0.376	–	0.29	0.24	0.14	Fe^2–$CaFe_2O_4$
95	0.374	517	–0.41	0.20	0.81	α-Fe_2O_3
	0.364	–	0.76	0.32	0.10	Fe^1–$CaFe_2O_4$
	0.356	–	0.27	0.23	0.09	Fe^2–$CaFe_2O_4$

[a] *IS* is the chemical isomeric shift relative to α-Fe, *QS*, quadrupole splitting, *W*, full width at half maximum of the Mössbauer line, and *A*, relative site occupancy.

Table 4. Mössbauer parameters of the $CaO–Fe_2O_3$ system catalysts (T_{syn} = 1000°C)

Fe_2O_3, wt %	*IS*, ±0.005 mm/s	*H*, ±5 kOe	*QS*, ±0.01 mm/s	*W*, ±0.01 mm/s	*A*, ±3%	Crystallographic position
55	0.364	509	–1.09	0.26	0.48	B–$Ca_2Fe_2O_5$
	0.183	435	1.43	0.24	0.47	A–$Ca_2Fe_2O_5$
	0.385	–	0.81	0.14	0.02	Fe^1–$CaFe_2O_4$
	0.383	–	0.32	0.28	0.04	Fe^2–$CaFe_2O_4$
60	0.364	509	–1.09	0.26	0.39	B–$Ca_2Fe_2O_5$
	0.180	434	1.43	0.24	0.39	A–$Ca_2Fe_2O_5$
	0.393	–	0.73	0.18	0.10	Fe^1–$CaFe_2O_4$
	0.390	–	0.29	0.26	0.13	Fe^2–$CaFe_2O_4$
65	0.364	509	–1.09	0.26	0.27	B–$Ca_2Fe_2O_5$
	0.180	434	1.43	0.24	0.26	A–$Ca_2Fe_2O_5$
	0.375	–	0.72	0.27	0.22	Fe^1–$CaFe_2O_4$
	0.373	–	0.30	0.26	0.25	Fe^2–$CaFe_2O_4$
70	0.360	509	–1.09	0.30	0.12	B–$Ca_2Fe_2O_5$
	0.178	435	1.45	0.25	0.12	A–$Ca_2Fe_2O_5$
	0.373	–	0.72	0.27	0.41	Fe^1–$CaFe_2O_4$
	0.374	–	0.29	0.27	0.36	Fe^2–$CaFe_2O_4$
74	0.383	517	–0.44	0.32	0.04	α-Fe_2O_3
	0.371	–	0.72	0.28	0.52	Fe^1–$CaFe_2O_4$
	0.369	–	0.29	0.26	0.45	Fe^2–$CaFe_2O_4$
78	0.383	517	–0.41	0.21	0.30	α-Fe_2O_3
	0.379	–	0.73	0.26	0.37	Fe^1–$CaFe_2O_4$
	0.376	–	0.29	0.26	0.33	Fe^2–$CaFe_2O_4$
80	0.382	517	–0.43	0.24	0.41	α-Fe_2O_3
	0.376	–	0.73	0.30	0.31	Fe^1–$CaFe_2O_4$
	0.375	–	0.29	0.26	0.28	Fe^2–$CaFe_2O_4$
85	0.381	517	–0.41	0.24	0.56	α-Fe_2O_3
	0.379	–	0.74	0.26	0.23	Fe^1–$CaFe_2O_4$
	0.376	–	0.30	0.26	0.21	Fe^2–$CaFe_2O_4$
90	0.380	516	–0.41	0.25	0.69	α-Fe_2O_3
	0.373	–	0.74	0.26	0.16	Fe^1–$CaFe_2O_4$
	0.372	–	0.31	0.24	0.15	Fe^2–$CaFe_2O_4$
95	0.383	518	–0.41	0.25	0.82	α-Fe_2O_3
	0.366	–	0.72	0.26	0.09	Fe^1–$CaFe_2O_4$
	0.359	–	0.30	0.24	0.09	Fe^2–$CaFe_2O_4$

spectroscopy studies. This concerns, in particular, the single-phase $CaFe_2O_4$ sample synthesized at 900°C under reduced partial oxygen pressure $P_{O_2} = 10^{-10}$ atm [32], as well as $CaFe_2O_4$ ferrite in the two-phase $CaFe_2O_4$–α-Fe_2O_3 samples synthesized in an air atmosphere at 1000°C [25]. As noted above, the α-Fe_2O_3 phase content in the $CaFe_2O_4$–α-Fe_2O_3 catalysts investigated in the present study widely varies from 1.5–2.0 to 81–82 wt % (Tables 1 and 2). The occupancy difference between the Fe^1 and Fe^2 crystallographic positions tends to increase with decreasing α-Fe_2O_3 content in the sample, suggesting that the hematite phase stabilizes the ferrite structure in the two-phase $CaFe_2O_4$–α-Fe_2O_3 samples. Redistribution of occupancies of the nonequivalent sites in the $Ca_2Fe_2O_5$–$CaFe_2O_4$ catalysts is obviously associated with the presence of the $Ca_2Fe_2O_5$ phase in the samples. Given strong quadrupole interactions (~10% of the magnetic interactions) characteristic of this phase, it can be assumed that polarization of the boundary $CaFe_2O_4$ layer at the interface by a strong electric field makes occupation of the Fe^2 sites energetically favorable.

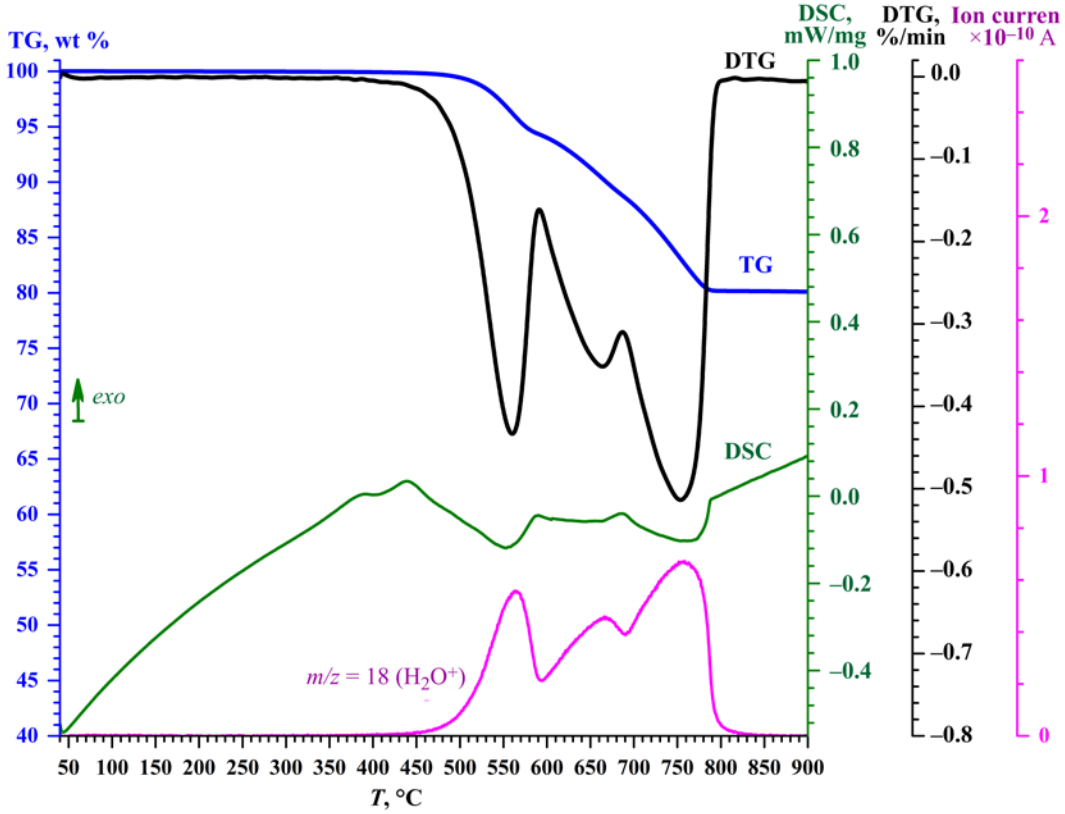

Fig. 2. TG, DTG, DSC, and MS (m/z = 18) curves for TPR of 65% Fe_2O_3 sample (T_{syn} = 900°C).

Iron vacancy states for other iron-containing phases in the catalysts were not revealed by the Mössbauer spectroscopy study.

Thus, the Mössbauer spectroscopy analysis of the two-phase catalysts from the $Ca_2Fe_2O_5$–$CaFe_2O_4$ and $CaFe_2O_4$–α-Fe_2O_3 regions showed that the synthesis of the samples at temperatures of 900–1000°C in an air atmosphere leads to formation of cation vacancies in the nonequivalent Fe sites in the $CaFe_2O_4$ ferrite structure.

Temperature-programmed reduction of the catalysts with hydrogen. It was of interest to elucidate how the revealed structural characteristics of calcium ferrites $Ca_2Fe_2O_5$ and $CaFe_2O_4$ in the composition of the CaO–$Ca_2Fe_2O_5$, $Ca_2Fe_2O_5$–$CaFe_2O_4$, and $CaFe_2O_4$–α-Fe_2O_3 two-phase samples affect the lattice oxygen reactivity with respect to hydrogen.

The oxidizing ability of the synthesized two-phase CaO–Fe_2O_3 system catalysts with respect to hydrogen was investigated in temperature-programmed reduction with hydrogen under simultaneous analysis of the mass loss, heat effects, and the formation of the hydrogen oxidation product. The reduction of the catalysts occurs as an endothermic mass-loss process in the temperature range 350–820°C in several stages. Figure 2 shows examples of the thermogravimetry (TG), differential thermogravimetry (DTG), and differential scanning calorimetry (DSC) curves and the mass spectrometry (MS) curve of the molecular ion H_2O^+ (m/z = 18), recorded during reduction of 65% Fe_2O_3 sample (T_{syn} = 900°C) containing 48% $Ca_2Fe_2O_5$, 52% $CaFe_2O_4$. It is seen that, in the temperature range 350–800°C, the DTG, DSC, and MS curves exhibit complex shapes with several extrema. The consistent run demonstrated by the complex-shaped DTG and MS curves indicates that the mass loss is associated with reduction of iron ions, involving lattice oxygen with different reactivities. Under the actual conditions, the iron-containing phases are completely reduced to the final products Fe^0 and CaO, as evidenced by reaching a plateau by the TG curve and by the occurrence of a second-order phase transition ferromagnetic α-Fe→paramagnetic β-Fe at the Curie temperature of 772–773°C (770°C [35]).

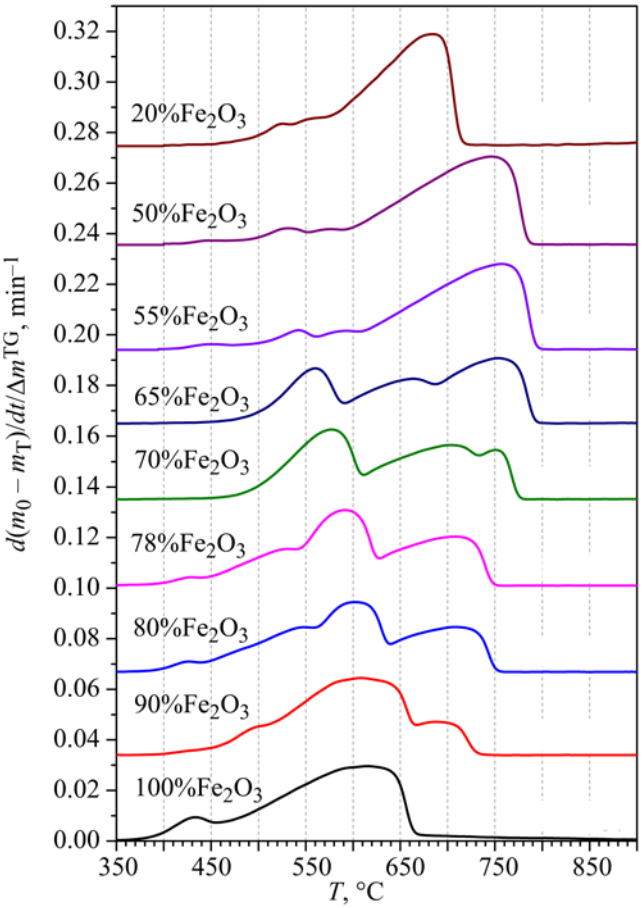

Fig. 3. Temperature dependence of the specific rate of mass loss due to the reduction of the CaO–Fe_2O_3 system catalysts (T_{syn} = 900°C), according to the DTG data.

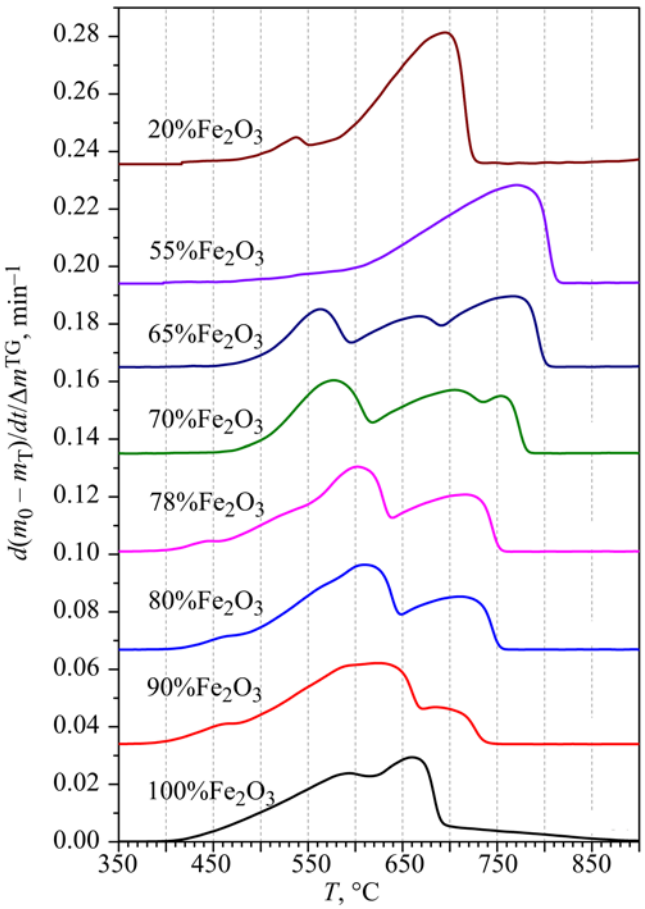

Fig. 4. Temperature dependence of the specific rate of mass loss due to the reduction of the CaO–Fe_2O_3 system catalysts (T_{syn} = 1000°C), according to the DTG data.

Figures 3 and 4 present the temperature-programmed reduction profiles of the samples with the Fe_2O_3 content varied from 20 to 100 wt %, which were synthesized at 900 and 1000°C. Comparison of the reactivities of the catalysts with respect to hydrogen was based on the specific rate of mass loss due to reduction of the samples, as demonstrated by the normalized DTG curves. As seen from Figs. 3 and 4, the reduction of the catalysts with the same composition, synthesized at two different temperatures, proceeds in a similar manner. The catalysts synthesized at 1000°C show a lower reactivity in hydrogen oxidation, as indicated by the shifts of T_{max} of the reduction peaks and of the complete reduction peaks toward higher temperatures.

As the Fe_2O_3 content in the CaO–Fe_2O_3 system changes, significant differences are observed in the temperature-programmed reduction profiles of the catalysts. The reduction curve for α-Fe_2O_3 oxide (Fig. 3) shows two peaks: a small peak with T_{max} 453°C, associated with the α-Fe_2O_3 reduction to magnetite, and a broad, poorly resolved peak in mid-temperature region (520–680°C) with T_{max} 615°C, which is due to the subsequent combined stages of oxides reduction to the metal [28]. The reduction of the sample is complete at 900°C.

With the appearance of the $CaFe_2O_4$ phase in the catalyst samples ($CaFe_2O_4$–α-Fe_2O_3 region) the TPR profiles display changes (Fig. 3). Specifically, there are two broad asymmetric peaks in the mid- and high-temperature regions and also a low-intensity low-temperature peak. For example, the reduction curve of 90% Fe_2O_3 sample (36% $CaFe_2O_4$, 64% α-Fe_2O_3), as compared to α-Fe_2O_3, exhibits a high-temperature peak with T_{max} 687°C, associated with removal of higher-

binding energy lattice oxygen species, and a weak peak in the range 460–520°C. With increasing content of the $CaFe_2O_4$ ferrite phase in the samples the contribution from the high-temperature component tends to increase, which evidences reduction of Fe ions in the calcium ferrite phase. The mass loss by the sample shows that, in the temperature range of interest, slightly less than half of the ferrite phase is reduced. This allows the mid-temperature asymmetric peak to be considered as resulting from superposition of the reduction peaks of the Fe ions in both hematite and ferrite phases. In the reduction curve of the sample containing 85 wt % $CaFe_2O_4$ (78% Fe_2O_3), the mid-temperature peak is slightly shifted to low temperatures, and also a weak low-temperature shoulder is observed. The TPR profiles of the $CaFe_2O_4$–α-Fe_2O_3 samples also exhibit a low-intensity low-temperature peak in the range 380–450°C, which is observed in reduction of 100% α-Fe_2O_3 sample as well. The reduction of the $CaFe_2O_4$–α-Fe_2O_3 samples is complete at 740–760°C. As noted above, these catalysts have a core-shell structure with α-Fe_2O_3 acting as the core. The shell around the ferrite core apparently limits the hydrogen access to α-Fe_2O_3. This leads to partial separation of the combined stages of the hematite reduction and to the appearance of an additional low-temperature peak in the case of 90% Fe_2O_3 catalyst, which shifts toward high temperatures with a decrease in the hematite content and with an increase in the ferrite content. The revealed TPR patterns of the $CaFe_2O_4$–α-Fe_2O_3 catalysts are consistent with the conclusions concerning stabilization of the ferrite structure by the hematite phase, made on the basis of the Mössbauer data.

In going to the $Ca_2Fe_2O_5$–$CaFe_2O_4$ catalysts, certain differences in reduction of the $CaFe_2O_4$ phase become evident (Fig. 3). In the TPR curves of the 65% and 70% Fe_2O_3 catalysts (52–83 wt % $CaFe_2O_4$, Table 2) there are three distinct peaks, specifically, a mid-temperature peak with T_{max} 560–577°C and a high-temperature peak, obviously consisting of two components, with T_{max} 664–703 and ~750–753°C; no low-temperature (below 450°C) peaks are observed. The appearance of a second higher-temperature component in the reduction curve and an increase in its contribution with increasing content of the $Ca_2Fe_2O_5$ phase indicate reduction of Fe ions in this ferrite. Basing on the phase composition and the mass-loss data for the samples, the two first-named peaks are attributable to the reduction of the $CaFe_2O_4$ ferrite phase. The reduction of the catalysts is complete at temperatures of 780–800°C. The shift of T_{max} of the mid-temperature reduction peak of $CaFe_2O_4$ in these samples to low temperatures compared to the reduction of $CaFe_2O_4$ in the $CaFe_2O_4$–α-Fe_2O_3 catalysts, containing, 73–85% $CaFe_2O_4$, is indicative of the influence of the $Ca_2Fe_2O_5$ phase.

When the $Ca_2Fe_2O_5$ ferrite phase content exceeds 80 wt % and the CaO phase appears in the catalysts (50 and 55% Fe_2O_3 samples, Table 2), an intense asymmetric broad high-temperature peak with T_{max} 747–757°C is observed in the reduction curves of the samples; it is associated with reduction of $Ca_2Fe_2O_5$, which evidently occurs in several sequential, poorly resolved stages (Fig. 3). The reduction of 4–9 wt % $CaFe_2O_4$ ferrite phase present in the samples is manifested as a low-intensity mid-temperature peak with T_{max} 576–592°C. Reduction of the samples is complete at 795–810°C.

Of particular note is the reduction of 20% Fe_2O_3 sample with the phase composition 69% CaO, 28% $Ca_2Fe_2O_5$, 3% $CaFe_2O_4$ (Fig. 3). It is seen that, compared to 50% Fe_2O_3 sample, $Ca_2Fe_2O_5$ ferrite exhibits a reduction peak that is significantly, by >60°C, shifted toward low temperatures and is characterized by T_{max} 684°C. Reduction of this sample is complete at a lower temperature (720°C) as well. Figure 4 shows that 20% Fe_2O_3 sample (68% CaO, 32% $Ca_2Fe_2O_5$) synthesized at 1000°C exhibits a similar reduction pattern. The data on the reduction of 20% Fe_2O_3 samples are indicative of the appearance in the $Ca_2Fe_2O_5$ phase of lattice oxygen species with enhanced reactivity compared to 50, 55% Fe_2O_3 samples. The crystal lattice parameters of $Ca_2Fe_2O_5$ ferrite in the CaO–$Ca_2Fe_2O_5$ catalysts vary with increasing ferrite content (Fig. 1). Considerable differences in the lattice parameters of $Ca_2Fe_2O_5$ between 20% and 50, 55% Fe_2O_3catalysts, containing 28–32% and 81–91% $Ca_2Fe_2O_5$, respectively, suggest that the higher reactivity of 20% Fe_2O_3 catalysts is due to the presence of sites in the disordered crystal structure of $Ca_2Fe_2O_5$.

CONCLUSION

Thus, the reduction of the CaO–Fe_2O_3 system catalysts from the CaO–$Ca_2Fe_2O_5$, $Ca_2Fe_2O_5$–$CaFe_2O_4$, and $CaFe_2O_4$–α-Fe_2O_3 regions, including iron oxide α-Fe_2O_3, synthesized at temperatures of 900 and 1000°C, was studied. It was shown that, for the two-phase samples, the reactivity with respect to hydrogen, exhibited by the lattice oxygen species in calcium ferrites $CaFe_2O_4$ and $Ca_2Fe_2O_5$, is influenced by the second phase, which

finding is in good agreement with the XRD and Mössbauer spectroscopy data. Specifically, the oxygen species in ferrite $CaFe_2O_4$ are more active in the samples from the $CaFe_2O_4$–$Ca_2Fe_2O_5$ compared to the $CaFe_2O_4$–α-Fe_2O_3 region, as evidenced by a 20–30°C shift of T_{max} of the mid-temperature reduction peak toward low temperatures. This may be due to the formation of cationic vacancies in the different nonequivalent crystallographic positions of iron in the $CaFe_2O_4$ ferrite structure, as established by the Mössbauer spectroscopy. In the CaO–$Ca_2Fe_2O_5$ samples the reactivity of the lattice oxygen species in ferrite $Ca_2Fe_2O_5$ depends on the phase ratio. The samples with CaO/$Ca_2Fe_2O_5$=2.2–2.4 are reduced at a lower temperature compared to those with a mass ratio of 0.05–0.20. The revealed differences between these catalysts in the crystal lattice parameters of $Ca_2Fe_2O_5$ suggest a decrease in the degree of the ferrite lattice disorder with a decrease in the CaO/$Ca_2Fe_2O_5$ ratio. Apparently, the activity of the CaO–$Ca_2Fe_2O_5$ catalysts is determined by the sites localized at the interface between CaO and the disordered crystal structure of $Ca_2Fe_2O_5$ and tends to decrease with decreasing degree of disorder of the ferrite lattice.

The results obtained may be useful for the development of calcium ferrites-based catalytic systems for high-temperature oxidation and cyclic processes such as fuel combustion, gasification of coal and biomass, hydrogen generation, etc.

EXPERIMENTAL

The CaO–Fe_2O_3 system catalysts were synthesized from extrapure grade Fe_2O_3 [TU (Technical Specifications) 6-09-1418-78] and pure grade CaO [GOST (State Standard) 8677-66)]. The reactants were mixed in the required proportion and ground with a KM-1 planetary ball mill for 1 h. The ground powders were pressed at $3.5 \cdot 10^3$ kg/cm^2 for 1.5–3 min to prepare the pellets with a diameter of 17 mm and a thickness of 1–2 mm. The obtained pellets were calcined at 900°C for 10 h, or at 1000°C for 4 h, and then cooled down to room temperature at a rate of ~8°C/min. Next, the pellets were crushed to a fraction of –0.2+0.1 mm. The samples were labeled as xx% Fe_2O_3, where xx is the weight content of Fe_2O_3 in the initial blend; e.g., 74% Fe_2O_3 sample contains 74 wt % Fe_2O_3, and 100% Fe_2O_3 sample corresponds to pure hematite treated according to the above-described procedure.

The specific surface area of the samples was determined using a NOVA 3200e sorption analyzer (Quantachrome Instruments, the United States) in the low-temperature nitrogen adsorption mode at –195.8°C. The specific surface area (S_{sp}) was calculated using the modified BET method in accordance with ISO standard [36].

Quantitative phase analysis and microstructural characterization of the samples were carried out on an X'Pert PRO MPD diffractometer (PANalytical, The Netherlands) with a PIXcel (CoK_α) solid-state detector using the Rietveld full-profile refinement and the derivative difference minimization method [37].

The state of the iron ions and the cationic distribution of iron in the phases over crystallographic positions were studied using room temperature Mössbauer spectroscopy in transmission geometry on an MS-1104Em spectrometer (Research Institute of Physics, Southern Federal University, Russia) with a Co^{57}(Cr) gamma ray source. The interpretation of the spectra was carried out similarly to [25].

Temperature-programmed reduction of the samples was conducted in a flow mode with a 5%H_2+95%Ar gas mixture at a feed rate of 100 cm^3/min on a Jupiter STA 449C simultaneous thermal analyzer coupled with an Aëolos QMS 403C mass spectral analyzer (Netzsch, FRG) at linear hearing rate of 5°C/min in the range 40–900°C. During the reduction, the mass (TG, DTG) and heat flux (DSC) changes and the mass spectrum of the molecular ion H_2O^+ (m/z = 18) were recorded. A sample of 30.0±0.1 mg weight was used for analysis. For more details on the experimental procedure, see [38]. Comparison of the reducing abilities of the samples was based on the specific rate of mass loss by the sample.

AUTHOR INFORMATION

N.P. Kirik, ORCID: https://orcid.org/0000-0002-4013-3444

V.V. Yumashev, ORCID: https://orcid.org/0000-0003-1407-1144

Yu.V. Knyazev, ORCID: https://orcid.org/0000-0001-9379-4628

L.A. Solovyev, ORCID: https://orcid.org/0000-0002-3905-3252

A.G. Anshits, ORCID: https://orcid.org/0000-0002-5259-0319

FUNDING

The study was carried out within the framework of the State Assignment of the Institute of Chemistry and Chemical

Technology, Federal Krasnoyarsk Research Center, Siberian Branch, Russian Academy of Sciences (project no. FWES–2021–0013).

CONFLICT OF INTEREST

No conflict of interest was declared by the authors.

REFERENCES

1. Shigapov, A.N., Novozhilova, M.A., Vereshchagin, S.N., Anshits, A.G., and Sokolovskii, V.D., *React. Kinet. Catal. Lett*., 1988, vol. 37, no. 2, p. 397. https://doi.org/10.1007/BF02062090
2. Roguleva, V.G., Nikiphorova, M.A., Maksimov, N.G., and Anshits, A.G., *Catal. Today*, 1992, vol. 13, p. 219. https://doi.org/10.1016/0920-5861(92)80145-D
3. Anshits, A.G., Voskresenskaya, E.N., and Shigapov, A.N., *Stud. Surf. Sci. Catal*., 1991, vol. 61, p. 49. https://doi.org/10.1016/S0167-2991(08)60062-2
4. Popovskii, V.V., *Kinet. Katal.*, 1972, vol. 13, no. 5, p. 1190.
5. Kremneva, A., Fedorov, A., Bulavchenko, O., Knyazev, Yu., Saraev, A., Yakovlev, V., and Kaichev, V., *Catal. Lett.*, 2020, vol. 150, no. 12, p. 3377. https://doi.org/10.1007/s10562-020-03250-8
6. Phillips, B. and Muan, A., *J. Am. Ceram. Soc*., 1958, vol. 41, no. 11, p.445. https://doi.org/10.1111/J.1151-2916.1958.TB12893.X
7. Shaula, A.L., Pivak, Y.V., Waerenborgh, J.C., Gaczynski, P., Yaremchenko, A.A., and Kharton, V.V., *Solid State Ionics*, 2006, vol. 177, p. 2923. https://doi.org/10.1016/j.ssi.2006.08.030
8. Tsipis, E.V., Pivak, Y.V., Waerenborgh, J.C., Kolotygin, V.A., Viskup, A.P., and Kharton, V.V., *Solid State Ionics*, 2007, vol. 178, p. 1428. https://doi.org/10.1016/j.ssi.2007.09.003
9. Ida, S., Yamada, K., Matsunaga, T., Hagiwara, H., Matsumoto, Y., and Ishihara, T., *J. Am. Chem. Soc*., 2010, vol. 132, p. 17343. https://doi.org/10.1021/ja106930f
10. Matsumoto, Y., Obata, M., and Hombo, J., *J. Phys. Chem*., 1994, vol. 98, p. 2950. https://doi.org/10.1021/j100062a035
11. Sutka, A., Kodu, M., Pärna, R., Saar, R., Juhnevica, I., Jaaniso, R., and Kisand, V., *Sens. Actuators (B)*, 2016, vol. 224, p. 260. https://doi.org/10.1016/j.snb.2015.10.041
12. Ahmed, M.G., Kandiel, T.A., Ahmed, A.Y., Kretschmer, I., Rashwan, F., and Bahnemcal, D., *J. Phys. Chem. C*, 2015, vol. 119, p. 5864. https://doi.org/10.1021/jp512804p
13. Hirabayashi, D, Yoshikawa, T., Mochizuki, K., Suzuki, K., and Sakai, Y., *Catal. Lett*., 2006, vol. 110, nos. 1–2, p. 155. https://doi.org/10.1007/s10562-006-0104-0
14. Isupova, L.A., Tsybulya, S.V., Kryukova, G.N., Budneva, A.A., Paukshtis, E.A., Litvak, G.S., Ivanov, V.P., Kolomiichuk, V.N., Pavlyukhin, Yu,T., and Sadykov, V.A., *Kinet. Catal.*, 2002, vol. 43, no. 1, p. 122. https://doi.org/10.1023/A:1014217716883
15. Ma, X., Feng, X., Guo, J., Cao, H., Suo, X., Sun, H., and Zheng, M., *Appl. Catal. B*, 2014, vol. 147, p. 666. https://doi.org/10.1016/j.apcatb.2013.10.003
16. Yu, Z., Yang, Y., Yang, S., Zhang, Q., Zhao, J., Fang, Y., Hao, X., and Guan, G., *Carbon Resour. Convers.,* 2019, vol. 2, p. 23. https://doi.org/10.1016/j.crcon.2018.11.004
17. Ismail, M., Liu, W., Dunstan, M.T., and Scott, S.A., *Int. J. Hydrogen Energy*, 2016, vol. 41, p. 4073. https://doi.org/10.1016/j.ijhydene.2015.11.066
18. Cheng, Z., Qin, L., Guo, M., Xu, M., Fan, J.A., and Fan, L., *Phys. Chem. Chem. Phys.*, 2016, vol. 18, p. 32418. https://doi.org/10.1039/C6CP06264D
19. Qin, L., Cheng, Z., Guo, M., Xu, M., Fan, J.A., and Fan, L.-S., *ACS Energy Lett*., 2017, vol. 2, no. 1, p. 70. https://doi.org/10.1021/acsenergylett.6b00511
20. Ismail, M., Liu, W., Chan, M.S.C., Dunstan, M.T., and Scott, S.A., *Energy Fuels*, 2016, vol. 30, no. 8, p. 6220. https://doi.org/10.1021/acs.energyfuels.6b00631
21. Zamboni, I., Courson, C., and Kiennemcal, A., *Appl. Catal. B*, 2017, vol. 203, p. 154. https://doi.org/10.1016/j.apcatb.2016.10.024
22. Siriwardane, R., Riley, J., Tian, H., and Richards, G., *Appl. Energy*, 2016, vol. 165, p. 952. https://doi.org/10.1016/j.apenergy.2015.12.085
23. Huang, B.-Sh., Chen, H.-Y., Chuang, K.-H., Yang, R.-X., and Wey, M.-Y., *Int. J. Hydrogen Energy*, 2012, vol. 37, p. 6511. https://doi.org/10.1016/j.ijhydene.2012.01.071
24. Xue, B.-J., Luo, J., Zhang, F., and Fang, Z., *Energy*, 2014, vol. 68, p. 584. https://doi.org/10.1016/j.energy.2014.02.082
25. Knyazev, Yu.V., Shishkina, N.N., Bayukov, O.A., Kirik, N.P., Solovyov, L.A., and Anshits, A.G., *J. Struct. Chem*., 2019, vol. 60, no. 5, p. 763. https://doi.org/10.1134/S0022476619050081
26. Berezhnoi, A.S., *Mnogokomponentnye sistemy oksidov* (Multicomponent Oxide Systems), Kyiv: Naukova Dumka, 1970, p. 97.
27. Isupova, L.A., Yakovleva, I.S., Tsybulya, S.V., Kryukova, G.N., Boldyreva, N.N., Vlasov, A.A., Alikina, G.M., Ivanov, V.P., and Sadykov, V.A., *Kinet. Catal.*, 2000, vol. 41, no. 2, p. 287. https://doi.org/10.1007/BF02771432

28. Kirik, N., Krylov, A., Boronin, A., Koshcheev, S., Solovyov, L., Rabchevskii, E., Shishkina, N., and Anshits, A., *Materials*, 2023, vol. 16, p. 4466:1. https://doi.org/10.3390/ma16124466
29. Fukuyama, H., Hossain, Kh., and Nagata, K., *Metall. Mater. Trans. B*, 2002, vol. 33, p. 257.
30. Leont'ev, L.I., Bogoslovskii, V.N., and Chufarov, G.I., *Zh. Neorg. Khim*., 1963, vol. 8, no. 1, p. 257
31. International Center for Diffraction Data, ICDD PDF #33–664. https://www.icdd.com/
32. Kharton, V.V., Tsipis, E.V., Kolotygin, V.A., Avdeev, M., Viskup, A.P., Waerenborgh, J.C., and Frade, J.R., *J. Electrochem. Soc*., 2008, vol. 155, no. 3, p. 13. https://doi.org/10.1149/1.2823458
33. McCammon, C.A., Becerro, A.I., Langenhorst, F., Angel, R.J., Marion, S., and Seifert, F., *J. Phys.: Condens. Matter*., 2000, vol. 12, p. 2969. https://doi.org/10.1088/0953-8984/12/13/308
34. Randhawa, B.S. and Sweety, K., *Bull. Mater. Sci*., 2000, vol. 23, p. 305. https://doi.org/10.1007/BF02720087
35. Weast, R.C., *Handbook of Chemistry and Physics*, Cleveland: Chemical Rubber Co., 1968–1969, p. E-117.
36. ISO 9277:2010-09(E)P: Determination of the Specific Surface Area of Solids by Gas Adsorption – BET Method, 2010.
37. Solovyov, L.A., *J. Appl. Crystallogr*., 2004, vol. 37, p. 743. https://doi.org/10.1107/S0021889804015638
38. Yumashev, V.V., Kirik, N.P., Shishkina, N.N., Knyazev, Yu.V., Zhizhaev, A.M., and Solovyov, L.A., *J. Sib. Fed. Univ. Chem*., 2019, vol. 12, no. 1, p. 54. https://doi.org/10.17516/1998-2836-0108